

The Influence of Substrate Lens Design in Terahertz Time-Domain Spectroscopy

J. Van Rudd

Picometrix, Inc., P. O. Box 130243, Ann Arbor, MI 48113

Daniel M. Mittleman

Electrical and Computer Engineering Dept., Rice University, MS-366, P. O. Box 1892, Houston
TX 77251-1892

Phone: (713) 348-5452 Fax: (713) 348-5686 E-mail: daniel@rice.edu

Abstract

We describe measurements of the angular radiation patterns from lens-coupled terahertz antennas fabricated on photoconductive substrates. These measurements have been performed using a novel terahertz time-domain spectrometer in which the femtosecond optical pulses used to gate the emitter and receiver antennas are delivered via optical fiber. We have used this system to perform a comparison between the two substrate lens designs commonly used in THz time-domain spectrometers. We have measured both E-plane and H-plane emission patterns for a 90° bow-tie antenna. By comparing these experimental results with simulations based on Fresnel-Kirchoff diffraction, we find that the choice of substrate lens design is important in determining not only the directivity of the emitted beam, but also the spectral bandwidth. These results emphasize the significance of this crucial component in the design of broadband THz spectrometers.

I. Introduction

Terahertz time-domain spectroscopy (THz-TDS) is a versatile technique for the generation and detection of radiation in the sub-millimeter range. It is by now well established that femtosecond optical pulses can be used to generate a spatially coherent beam of terahertz radiation, in the form of single-cycle electromagnetic pulses. This unique tool has been exploited in spectroscopic studies of a wide range of material systems [1] since its development in the late 1980's [2, 3]. Recently, a variety of imaging and sensing capabilities have been explored, which have illustrated the potential value of the technique in manufacturing and quality control applications [4]. These demonstrations have spurred the development of a commercial THz imaging system, the first of its kind [5]. As a result of the growing importance of this technique, much research has been devoted to characterizing the terahertz beam. Early characterization efforts concentrated on issues such as the achievable bandwidth and the sources of noise in photoconductive sampling measurements [3, 6]. A more complete system characterization accounted for factors such as the collection optics and the spectral response of the dipole antennas used for both generation and detection [7]. More recently, there has been substantial interest in the use of THz-TDS as a tool for the study of ultra-broadband pulse propagation [8-11].

Despite this considerable interest in the characterization of THz-TDS, there have been few reports in which the spatial variation of the THz beam has been studied [12-15]. As a result, there are several aspects of the optical systems commonly used for THz time-domain spectroscopy and imaging systems in which the optimization has not been thoroughly performed. One important example is the design of the substrate lens. In the most common implementation of THz time-domain spectroscopy, the emitter and receiver antennas are lithographically defined

on photoconductive substrates. These substrates are then glued to high-resistivity silicon substrate lenses, which efficiently couple the THz radiation into (and out of) free space. The use of a substrate lens coupled to a planar antenna was pioneered by Rutledge and co-workers [16, 17], and has subsequently become very popular [18-20]. Grischkowsky and co-workers first described the use of a substrate lens to improve the performance of THz-TDS systems [2, 21], and these improvements have been discussed by a number of authors [4, 6, 7, 22]. In most THz-TDS systems, two distinct lens designs have been widely used, both borrowed from earlier microwave and millimeter-wave techniques. In one, the collimating lens, the emitter is located at the focus of the substrate lens [23]. In the other, the hyperhemisphere, the emitter is located so that a minimum of the emitted rays are lost to internal reflection inside the lens [17]. This latter design produces a beam with no spherical aberration or coma, and is therefore aplanatic.

Although both lens designs have been used extensively for many years, it is only relatively recently that direct comparisons have been performed. Several groups have described simulated and experimental results for the parameters of the beam emerging from the lens, as a function of the (cylindrical) extension of the lens beyond hemispherical [24-26]. These results cover cases similar, though not identical, to the two lens designs mentioned above. However, most of this work has been concerned with the generation or detection of narrowband emission. The situation in which the emitted radiation is broadband, of particular relevance to THz time-domain spectroscopy, has not been addressed. As a result, the dramatic influence of the substrate lens design on the achievable bandwidth in THz-TDS system has not been generally appreciated.

Here, we describe an experimental comparison of the spatial and spectral radiation patterns generated by the two most common substrate lens designs. We employ a substrate lens with a radius chosen to permit easy and rapid switching between the two configurations. This

facilitates a direct comparison of both the E-plane and H-plane emission from the two lens designs. These measurements have been performed using a fiber-coupled THz antenna module, which offers a number of unique advantages. First, it permits easy repositioning of the detector without loss of either optical alignment or absolute temporal delay. Because it is not necessary to re-align the optical beam onto the antenna each time it is moved, many measurements can be made in a relatively short time, minimizing the effects of system drift. An even more important advantage afforded by the fiber-coupling is that one may mount the detector on the end of a rail which pivots around the position of the emitter, as shown in figure 4 below. This guarantees that the receiver antenna is always oriented normally to the propagation direction of the emitted wave. As a result, the angular sensitivity of the receiver antenna is not a factor in these measurements. This is in contrast to the early measurement of Jepsen and Keiding, in which the antenna was translated along a line transverse to the optical axis of the radiated wave [13]. In the results presented here, the data reflects the angular distribution of the emitted radiation, rather than a convolution of the emitter and receiver antenna patterns. We compare our results with simulations based on scalar wave Fresnel-Kirchoff diffraction theory. This theoretical approach is described in section II, the aplanatic and collimating lens designs are reviewed in section III, and the experimental results are presented in section IV and discussed in section V.

II. Simulations

We simulate the emission process in the manner described by Jepsen and Keiding [13, 27]. First, the radiation pattern of the free-space antenna is modified by the presence of a high-dielectric substrate. The modification of a dipole pattern due to a nearby dielectric interface is a well known result, that can be expressed analytically [28], and that has been verified by

experiment [29]. In the measurements reported here, we employ a bow-tie emitter antenna. There is no equivalent closed-form expression for either a free-space bow-tie or a bow-tie on a dielectric substrate, although the emission from bow-tie antennas has been studied both theoretically and experimentally for many years [17, 30-32]. We note that the radiation patterns for a bow-tie and a dipole antenna are not too different from one another [17]. Also, as demonstrated below, the measured radiation patterns are determined much more by diffraction effects at the exit aperture of the substrate lens than by the antenna pattern inside the substrate. We therefore expect that the results presented here, although specific to the bow-tie geometry, reflect trends that are generally applicable to most commonly used lens-coupled THz emitters. As with dipole antennas, most of the radiated energy from a bow-tie antenna on a high dielectric substrate is directed into the substrate [17, 31]. This distorted, angle-dependent emission pattern then propagates to the inner surface of the substrate lens. In the model, we ignore the small index discontinuity at the interface between the GaAs substrate ($n_{\text{GaAs}} = 3.61$) and the silicon lens ($n_{\text{Si}} = 3.418$), by assuming that the entire structure has an index equal to that of silicon [33].

Once the field on the inner surface of the substrate lens is known, then the external field can be calculated by accounting for refraction through the interface, and diffraction through the finite aperture presented by the lens. This diffraction produces a complicated, frequency-dependent pattern in the far field of the emitter, which can be described using a Fresnel-Kirchoff diffraction calculation [13]. The amplitude at a position \mathbf{r} in the far field can be calculated by summing the contributions from every point \mathbf{r}_0 on the external surface of the hemispherical substrate lens, according to:

$$E(\mathbf{r}) \propto \iint dA E(\mathbf{r}_0) \cdot \frac{e^{ikr}}{r} [\cos(\mathbf{n}, \mathbf{r}) - n_{\text{Si}} \cos(\mathbf{n}, \mathbf{r}_0)] \quad (1)$$

The factor $E(\mathbf{r}_0) \cdot e^{ikr}/r$ is a secondary wavelet originating from the surface element $dA =$

$R^2 \sin\theta d\theta d\phi$ of the lens. The integral is performed over the entire surface of the substrate lens, generally not precisely half of a sphere because of the finite thickness of the substrate and the displacement of the antenna from the lens center. The factor in the square brackets, known as the inclination factor, depends on the inwards-pointing surface normal \mathbf{n} [23].

This formalism makes a number of simplifying assumptions. First, the vector nature of the field is neglected, so no information about the polarization of the diffracted wave can be obtained. Gürtler *et al.* have recently noted that a full vector field diffraction theory is necessary in certain situations, such as in the case of near-field propagation when the wave fronts curvature approaches the wavelength of the radiation [34]. In the present case, this is not likely to be an important consideration. Second, it is assumed that all relevant dimensions are much larger than the wavelength. This assumption is not violated despite the broadband nature of the THz pulses investigated here. In our data, the lowest measured frequency component (~ 100 GHz) has a wavelength of approximately 0.88 mm in the silicon lens, about a factor of 5 less than the lens radius. A more significant approximation is necessitated by the fact that our emitting antennas are bow-ties. The bow-tie pattern has been measured by a number of researchers, and can be calculated using finite element analysis [17, 31], but there is no analytic expression for the result. Instead, we compute the radiated field using a dipole emission pattern as the starting point. As noted above, the result for the bow-tie is not dramatically dissimilar from that of a conventional dipole pattern [17], so the calculations provide a useful starting point for understanding the data.

Figure 1 illustrates the geometry of a bow-tie emitter antenna, and the coordinate system used throughout this paper. The x-axis points along the axis of the dipole, and defines the predominant polarization axis of the emitted radiation. The z-axis is the optical axis, pointing through the center and tip of the substrate lens (not shown). The angle ϕ , the opening angle of

the emitting bow-tie antenna, is 90° in all of these experiments. Using the experimental arrangement shown in figure 4 below, it is possible to measure any of the four possible polarization combinations: the s- and p-polarized E-plane (in the plane of the dipole), as well as the s- and p-polarized H-plane (perpendicular to the plane of the dipole).

It is important to note that these calculations do not provide an accurate description of the relative amplitudes of different frequency components within the measured THz wave. These relative amplitudes are determined, not only by the interference of the diffracting beam, but also by such factors as the duration of the optical pulses used to gate the antennas, the carrier lifetime in the detector antenna, and the size of the emitter and receiver dipoles [7]. None of these factors are included in these simulations. Nonetheless, it is instructive to see how much of the frequency response is determined solely by the diffraction effects modeled here.

III. Substrate Lens Design

Figure 2 shows ray tracing diagrams for the two common substrate lens designs studied here. These diagrams are shown to scale for the experimental geometry explored here, with $R = 4$ mm substrate lenses. In the case of the collimating hemisphere, the emitter is at the focus of the substrate lens, so the rays emerge from the lens as a nearly collimated beam. At large angles the internal incidence angle approaches the critical angle for total internal reflection, leading to a strongly refracted ray and an aberrated wavefront. At still larger angles, radiation is trapped inside the lens, as shown by the dashed rays in figure 2a. For this design, the distance from the emitter to the tip of the lens is given by:

$$d_{\text{collimating}} = R \left(\frac{n}{n-1} \right) \quad (2)$$

where n is the refractive index of the lens. In the case of silicon, $d_{\text{collimating}}$ is approximately

1.41·R. The other design, the aplanatic hyperhemisphere, places the emitter at a position so that no rays are trapped by internal reflections. The emitter-to-lens-tip distance is:

$$d_{\text{hyper}} = R \left(\frac{n+1}{n} \right) \quad (3)$$

For silicon, $d_{\text{hyper}} = 1.29 \cdot R$. The aplanatic lens decreases the effective f-number of the antenna system by a factor of n , relative to the system without a substrate lens [17]. In this case, the radiation emerges as a diverging beam, with a $\sim 30^\circ$ cone angle, and with no wavefront aberration. However, the finite size of the antenna substrate (2 mm square in the present case, as shown in figure 2), prevents rays at large angles from escaping the emitter. Because of the very different beam divergence angles in the two cases, it is not clear *a priori* which design is more efficient for THz generation. Of course, these ray diagrams neglect the effects of diffraction, which, as shown below, are extremely important in these systems.

The implications of the substrate lens design are most important when considering the optical system used to collect and manipulate the THz beam [2, 4, 7]. For example, a common design would be to place a free-space collection lens or off-axis parabola in front of the emitter, to produce a collimated beam. In the case of the collimating substrate lens, the need for this collection lens can only be understood if diffraction is included, since in the ray optics description this beam is already collimated. Since the wavefront that reaches the collection lens is strongly perturbed by diffractive effects, the beam after the collection lens has a frequency-dependent transverse spatial profile. Radiation with higher frequencies propagates closer to the optical axis. If this beam is re-imaged using a second free-space lens, the resulting focal spot is frequency-independent, which can be advantageous for such applications as coupling into waveguides, for example [35]. On the other hand, for the case of the aplanatic substrate lens, one might imagine that the beam is less affected by diffraction, since it emerges as a diverging

source (see figure 2). In this case, the beam after the collection lens has a transverse profile that is independent of frequency [4]. Re-imaging the beam produces a focal spot with a strongly frequency-dependent diameter. This can be exploited to improve resolution in imaging applications [36]. Also, in the ray optics picture the beam after the collection lens is collimated in one case, but comes to a beam waist quite rapidly in the other. This could have important implications for the design of a THz system, since it would dictate the required separation between the emitter and receiver antennas [6]. However, when diffraction effects are included, it is no longer clear that this distinction is important.

Figure 3 shows examples of calculations performed as described above. These show the p-polarized E-plane and s-polarized H-plane angular emission patterns at a frequency of 0.5 THz, assuming a transmitter-to-receiver separation of 50 cm and a silicon aplanatic hyperhemispherical substrate lens with a radius of 4 mm. This figure shows the results for the two different substrate lens designs, demonstrating a dramatic difference between them. It also shows the angular distribution for a dipole on a silicon substrate, undistorted by diffraction and interference effects. This is the pattern one would measure if the emitter were located at the exact center of the hemispherical substrate lens, so that no refraction occurs at the lens surface. Hints of this pattern remain only in the case of the hyperhemispherical lens.

IV. Experimental Results

Figure 4 shows a schematic of the experimental arrangement used in these measurements. With the exception of the fiber coupling this is a fairly conventional THz-TDS system [4, 7], using laser pulses of approximately 100 femtoseconds duration at a repetition rate of 80 MHz. These pulses are pre-compensated for group velocity dispersion prior to being injected into the

single-mode optical fiber. The fiber is split into two arms, one for the transmitter and one for the receiver. The pulses in the receiver arm exit the fiber, pass through a computer-controlled optical delay, and are coupled back into fiber. The delay consists of a long rail that provides up to 1 nanosecond of delay, as well as a rapid scanning delay line [4, 37], that permits measurement of THz waveforms within a 40 picosecond window at a rate of 20 Hz. The optical power in the fiber is kept below 10 mW to avoid nonlinear pulse broadening. Even so, a signal-to-noise of 1000 per sweep of the scanning delay line is not unusual. As noted above, the receiver antenna is mounted on the end of a rail that pivots around the position of the emitter antenna. The photographs in figure 5 show the mounting chuck for the (stationary) emitter antenna (figure 5a) and the fiber-coupled receiver antenna module (figure 5b). For the emitter, the more cumbersome mounting is used to permit easy exchange of the substrate lens.

For the measurements reported here, the receiver antenna is a 90° bow-tie, fabricated on low-temperature-grown GaAs. It is positioned a fixed distance from the emitter. A wire-grid polarizer is positioned directly in front of the receiver, oriented to pass radiation polarized parallel to the receiver orientation. Although the receiver has a small sensitivity to cross-polarized radiation, the polarizer effectively filters out any such components, so the measured radiation is purely linearly polarized [14, 15]. At each angle θ relative to the optical axis (the z axis in figure 4), 1000 waveforms are averaged using the scanning delay line. The detector is then manually repositioned at a different angle. In this manner, the emitted electric field $E_{\text{THz}}(t;\theta)$ is measured directly. Fourier transform of these waveforms produces the complex spectrum $E_{\text{THz}}(\omega;\theta)$. Both the amplitude and phase of the radiated field are extracted from these measurements.

In order to rapidly switch between the two different lens designs, a substrate lens radius

of 4 mm is chosen. From equations (2) and (3) above, we find that the optimum distance from the emitter to the lens tip is approximately 5.7 mm for the collimating lens, and 5.2 mm for the hyperhemispherical case. One can therefore switch rapidly between these two cases with a lens cut for the hyperhemispherical design and a circular silicon plate of approximately 0.5 mm thickness. Inserting this flat disk between the lens and the substrate increases the antenna-to-lens-tip distance by almost precisely the appropriate amount. If this disk is at least 4 mm in radius, then it does not interfere with the waves propagating within the silicon, assuming that all surfaces are in optical contact. In order to insure that the substrate lens is aligned correctly, a real-time alignment procedure is employed. The THz waveform is optimized by manual positioning of the lens, and then affixed in place prior to subsequent measurements.

Figure 6 shows measured E-plane waveforms (p-polarized), at several different angles, for the (a) hyperhemispherical and (b) collimating substrate lens. Here, the emitter-to-detector distance is 26 cm. This distance was chosen as a trade-off between diminishing signal and improving angular resolution with increasing distance. We estimate an angular resolution of $\sim 2^\circ$ in these measurements. In both (a) and (b), the waveform broadens and shifts to increasing delay as the angle increases. However in the hyperhemispherical case the waveforms are initially more symmetric, and they lose their high frequency components more rapidly. The details of the pulse broadening are also quite distinct. Figure 7 summarizes these data in the frequency domain, and figure 9 shows a similar summary for the s-polarized H-plane results. In figures 7b and 9b, the persistence of higher frequency components at low angles is more noticeable. Figure 8 shows cuts through the data of figure 7, which clearly demonstrate this persistence. Along the optical axis, the collimating geometry provides substantially more bandwidth. Because of the different divergence properties of the two lens designs, this effect is reversed even at angles of only 10° , as

shown in figure 8. These results can be understood directly from the ray diagram (figure 2), which is increasingly valid at higher frequencies. Also, figures 7-9 illustrate the pronounced interference fringes at large angles in both cases.

We note that the data of figures 7 and 9 are plotted on a common vertical axis, to facilitate comparisons of relative amplitudes. The peak field radiated by the hyperhemispherical lens is about 20% larger than the peak field in the collimating case. The total radiated energy in the hyperhemispherical case, integrated over angle and frequency, is almost 80% larger in the E-plane, and about 50% larger in the H-plane. Figure 10 shows the radiated energy in the E-plane as a function of angle, integrated over all the frequency components shown in figures 7. The narrower angular emission in the case of the collimating lens is clearly shown. The integrated H-plane emission shows behavior similar to the E-plane results shown in figure 10. Bray and Roy have pointed out that the aplanatic hyperhemisphere exhibits a lower reflection loss than other extended hemispherical lens designs, consistent with these results [26]. The solid and dashed lines in figure 10 show the results of simulations of these integrated angular emission plots, calculated as described above. Here, the simulation of the hyperhemispherical lens is scaled to coincide with the experimental data point at zero degrees, and the result for the collimating lens is scaled by the same factor. The agreement between the simulations and the data is reasonably good for angles larger than about 5° . The disagreement at small angles in the case of the collimating lens can be understood by examining a calculation of the full spectral dependence of the angular emission.

One of the unique aspects of THz time-domain spectroscopy is its ability to measure the THz electric field coherently, and thus preserve the phase information. As a result, it is possible to determine not only the amplitude of $E(\omega; \theta)$, but also its phase. In doing so, one finds that the

spectral phase is dominated by a term that varies linearly with frequency, of the form $-\omega\tau$. This arises from the arbitrary assignment of $t = 0$ in the waveform measurements. In order to display the phase variation with frequency, we remove this uninteresting component by fitting a linear function to the spectral phase at $\theta = 0$. This linear function is then subtracted from the phase at all angles, and the residual is shown in figure 11 for the E-plane emission. The results for the hyperhemispherical lens are shown in (a), while the results for the collimating lens are shown in (b). Just as seen above, the characteristic radiation patterns inside the lens is no longer discernable. In particular, the expected $\pi/2$ phase jump at the critical angle of $\sim 17^\circ$, associated with the discontinuities visible in figure 3, are obscured by the effects of diffraction [17]. However, the differences between the two phase patterns are more pronounced than in the amplitude spectra. In the former, weak interference fringes are visible, and these appear to be dependent on both frequency and angle in a manner similar to those in figure 7a. In the latter, the overall phase change at large angle is much larger. (Note the difference in the vertical axes in these two plots.) This may be the result of the strong refraction of rays near the critical angle, as depicted in figure 2. Because this phase distortion occurs only at fairly large divergence angles, it will not have a marked influence on the collected THz beam unless very low $f/\#$ optics are used. Even in this case, the relative amplitude of this contribution to the overall THz signal is quite small.

V. Discussion

Figure 12 shows the results of such diffraction calculations, simulating the E-plane data of figure 7. Here, it is clear that, even in the absence of any other mechanism that could limit the measured THz bandwidth, the geometry of the substrate lens can have a dramatic effect. In the

case of the hyperhemispherical lens, the spectral content is limited to ~ 0.6 THz even in the forward direction ($\theta = 0^\circ$), in approximate agreement with the experiment (figure 7a). With a collimating lens design, the geometry does not place any limits on the bandwidth along the optic axis, at least up to 1 THz. Of course, the experimentally measured spectral bandwidth is limited by factors other than the diffraction geometry, which as mentioned above are not included in this simulation.

The achievable bandwidth in a THz system can be limited not only by the choice of lens design, but also by the size of the substrate lens. To study this phenomenon, we perform simulations to determine the spectral amplitude of the radiation emitted in the forward direction, at $\theta = 0^\circ$. Figure 13 shows the results of these simulations, for several different lens radii and both lens designs. In both cases, the spectral width decreases as the lens radius increases, as the spectrum becomes richer in low frequency components. A larger lens presents a larger aperture to the emitted THz beam, and therefore leads to less diffraction for a given wavelength. As a result, the amplitude of the low frequency components along the optic axis grow as the lens radius increases. As one might expect from the divergence properties of the two lens designs, this process is much more dramatic in the case of the hyperhemispherical lens. Also, the total radiated power in the forward direction increases more rapidly for the collimating design. It should be noted that, for lenses as small as 2 mm radius, the wavelength of 100 GHz radiation inside the lens approaches the size of the lens, so the accuracy of these simulations is questionable in this limit.

The simulations shown in figure 12 also provide useful insight into the divergence of the emitted THz beam. For the hyperhemispherical lens, the spectral content of the beam is spread over a cone with a half-angle of $\sim 15^\circ$ at the higher frequencies, as expected from the ray tracing.

For the collimating lens, a majority of the energy propagates within a cone of only a few degrees, except for the lowest frequencies. The degree of collimation of the emitted beam can be expressed in terms of the directivity. We calculate the directivity from the measured radiation patterns according to:

$$D(\nu) = \frac{2 \cdot \max \left[|E_{\text{THz}}(\theta)|^2 \right]}{\int |E_{\text{THz}}(\theta)|^2 \sin \theta d\theta} \quad (4)$$

where $|E_{\text{THz}}(\theta)|$ represents the measured spectral amplitude at a given frequency ν , and the factor of 2 is a normalization for the angular integral [38]. Figure 14 shows the directivity calculated from the data of figures 7 and 9. For higher frequencies, the directivity is substantially larger for the collimating lens, and increases with increasing frequency, as expected for a diffraction-limited beam. In contrast, the hyperhemispherical lens shows an almost frequency-independent result, also as expected from the considerations mentioned above. The data from the hyperhemispherical lens also manifest a small but measureable peak near 200 GHz, in both the E-plane and the H-plane. This results from a strong interference fringe that occurs near this frequency at small angles. The solid lines in figure 14 show the directivity computed from the simulated patterns shown in figure 12. These reproduce many of the features of the experimental results.

Filipovic *et al.* have commented on the optimization of the lens design for a quasi-optical system of the type commonly used in time-domain spectrometers [24]. In this work, it was noted that the aplanatic design provides a lower directivity, and thus requires a small $f/\#$ optical system for efficient collection. In contrast, a collimating lens similar to the one considered here has a more highly directional beam (with increasing directivity at higher frequencies), and therefore requires a higher $f/\#$ system, which is easier to align. They also calculated the overlap between

the emitted radiation and an ideal Gaussian beam, which can be taken as a measure of the efficiency with which this radiation can be coupled into a Gaussian-beam optical system. This coupling efficiency is computed according to:

$$\eta(\nu) = \frac{\left| \int E_{\text{THz}}(\theta) \cdot e^{-\left(\frac{\theta}{\theta_0}\right)^2} \sin \theta d\theta \right|^2}{\left[\int |E_{\text{THz}}(\theta)|^2 \sin \theta d\theta \right] \left[\int e^{-2\left(\frac{\theta}{\theta_0}\right)^2} \sin \theta d\theta \right]} \quad (5)$$

The parameter θ_0 defines the width of the ideal Gaussian beam. In performing the calculation, the efficiency η is optimized with respect to θ_0 for each frequency component. The result showed that an aplanatic lens has a relatively high Gaussian coupling, whereas a collimating lens has a lower coupling that decreases with increasing frequency. In other words, a more highly directional beam couples less efficiently to a Gaussian mode. On the basis of these findings, Filipovic and co-workers recommended a compromise lens design, with an emitter-to-lens-tip distance of between 1.32 and 1.35 times the lens radius [24]. This is approximately the geometric mean of d_{hyper} and $d_{\text{collimating}}$ as defined above, and should provide a reasonably directional beam with good Gaussian coupling. Figure 15 shows the Gaussian coupling efficiency calculated from the E-plane data of figure 7 using equation (5). We observe that the hyperhemispherical lens has a higher coupling efficiency over most of the accessible spectral range, reaching as high as 94% near 600 GHz, consistent with the results of Filipovic *et al.* However the distinction between the two lens designs is not as pronounced in our results, possibly due to the difference between the synthesized ellipsoidal lenses used in the earlier work and the truncated spherical lenses employed here.

VI. Conclusions

We have reported detailed measurements of the angular radiation patterns of broadband terahertz photoconductive antennas. These are compared with simulations based on a Fresnel-Kirchoff diffraction calculation. The results confirm several pieces of conventional wisdom in the field of terahertz time-domain spectroscopy, and also provide some new insight. As reported by Jepsen and Keiding, we find that the radiated terahertz field is largest along the optical axis, with significant interference fringes at larger angles, resulting from the diffraction of the radiation through the aperture presented by the substrate lens [13]. As one might suppose from a simple ray diagram analysis, the radiated THz energy propagates more in the forward direction when a collimating lens geometry is employed. However, the total emitted energy is somewhat reduced, possibly because of the fact that some portion of the radiation is trapped inside the substrate lens by total internal reflection. In addition, the $\sim 30^\circ$ divergence angle expected for the hyperhemispherical lens design is also confirmed.

The choice of substrate lens is an important factor in the design of the optical system used to collect and transport the THz beam. The aplanatic design provides a nearly frequency-independent directivity that is quite low, and thus requires low $f/\#$ optics for high efficiency. On the other hand, the beam is somewhat more closely matched to a Gaussian mode, which can compensate for some of the losses associated with the high divergence. The suggestion of Filipovic *et al.* [24] to use a lens that is intermediate between the two cases studied here has not been implemented in THz-TDS systems. This could be an important method for optimizing the efficiency and signal-to-noise in these spectrometers.

One of the unanticipated results from the comparison between the two lens designs involves their influence on the measured THz bandwidth. From the simulations, it appears that the collimating lens places much weaker restrictions on the bandwidth of the emitted radiation;

instead, the bandwidth is limited by other factors such as the properties of the photoconductive sampling detector or the duration of the optical pulse used to gate the emitter. In contrast, when a hyperhemispherical lens is used, the bandwidth is dramatically limited by the diffraction geometry, as the radiated wave exhibits large interference fringes even in the forward direction. This highlights an important and usually neglected factor in the optimization of the bandwidth for spectroscopic measurements. Additional simulations and experiments will be required to study the effects of intermediate lens designs on the bandwidth of lens-coupled THz emitters.

We wish to acknowledge the assistance of P. U. Jepsen and T. D. Dorney in the implementation of the diffraction calculation. This work has been supported in part by the National Science Foundation and the Environmental Protection Agency.

Figure Captions

Figure 1 Schematic of the bow-tie emitter used in these measurements, along with definitions of the coordinate system employed throughout this paper. The opening angle of the bow-tie is $\phi = 90^\circ$ in these measurements.

Figure 2 Ray tracing diagrams of the two lens designs studied in this work. The upper diagram shows the collimating lens design. The aberration of the wavefront, arising from rays propagating close to the critical angle inside the lens, is evident. Rays represented by dashed lines are those that are trapped inside the lens by total internal reflection. The lower diagram shows the hyperhemispherical lens design, in which no rays are internally reflected, and the emitted radiation emerges with a divergence half-angle of about 15° and no wavefront aberration. These diagrams are shown to scale for a substrate lens of 4 mm radius, with a refractive index equal to that of silicon, $n_{\text{Si}} = 3.418$. In both cases, the antenna is fabricated on a 2 mm-square GaAs substrate, also shown. In the hyperhemispherical design, a substrate of this size can interfere with the propagation of radiation at large angles, and may decrease the emission efficiency as a result. The diagrams neglect the small index difference between GaAs and Si.

Figure 3 Sample simulations showing the angular emission patterns in (a) the E-plane and (b) the H-plane, for the two lens designs. The dotted line, denoted as ‘hemispherical’ in these plots, shows the result for the radiation pattern inside the lens. This is equivalent to what one would measure if the emitter were located at the center of an ideal hemispherical substrate lens. The

discontinuities in these patterns at 17° result from internal reflection at the air-substrate interface.

Figure 4 Schematic of the setup used in these measurements. The system is a conventional THz time-domain spectrometer, except that both photoconductive antennas are fiber-coupled, as shown. This permits easy repositioning of the receiver without loss of alignment or temporal synchronization.

Figure 5 Photographs of the fiber-coupled (a) emitter and (b) receiver module. The more cumbersome emitter chuck is used to facilitate replacement of the substrate lens. The receiver module is hermetically sealed, with a substrate lens protruding from the left side in this image and electrical connections for measuring the induced photocurrent. The E-plane and H-plane can be measured simply by rotating both antennas.

Figure 6 Typical E-plane waveforms, for the (a) hyperhemispherical and (b) collimating lens designs. The emission angles are shown in the plots. Waveforms from the H-plane show very similar behavior, in both cases.

Figure 7 Amplitude spectra of the measured waveforms as a function of both frequency and emission angle. (a) E-plane emission from an antenna coupled to a hyperhemispherical lens. (b) E-plane emission from an antenna coupled to a collimating lens. These data and the data of figure 9 are all shown on a common vertical axis, to facilitate comparisons of relative amplitudes.

Figure 8 Spectral cuts through the data of figure 7, at two different angles, shown on a log scale. The upper two curves show the data collected along the optic axis, while the lower two curves show the data collected at an angle of 10° . These latter two curves have been vertically displaced downwards by a factor of 10, for clarity. In the forward direction the collimating lens design provides more signal at high frequency; in the off-axis direction, the collimating nature of this lens design reduces the measured bandwidth more rapidly than in the aplanatic case.

Figure 9 Amplitude spectra of the measured waveforms as a function of both frequency and emission angle. (a) H-plane emission from an antenna coupled to a hyperhemispherical lens. (b) H-plane emission from an antenna coupled to a collimating lens. These data and the data of figure 7 are all shown on a common vertical axis, to facilitate comparisons of relative amplitudes.

Figure 10 Power emitted in the E-plane integrated over all frequency components shown in figure 7, as a function of emission angle. Solid squares show the results for the hyperhemispherical lens design, while open squares show the results for the collimating design. The solid and dashed lines are the results of simulations of the integrated power, for the hyperhemispherical and collimating cases, respectively. These simulated results have been scaled by a common factor, chosen so that the curve for the hyperhemispherical case coincides with the data point at an angle of zero degrees.

Figure 11 Experimentally determined spectral phase of the THz waveforms measured in the E-plane. The data are shown as a function of frequency and angle, for (a) the hyperhemispherical

lens design, and (b) the collimating lens design. Note the different vertical axes in the two plots. The collimating lens introduces a much larger phase distortion at large angles, which is probably related to the wavefront aberration shown in the ray tracing diagram (figure 2).

Figure 12 Simulation of the full E-plane emission pattern as a function of both angle and frequency, for (a) the hyperhemispherical lens design, and (b) the collimating lens design. The hyperhemispherical lens introduces strong interference fringes even at zero degrees, limiting the measureable emission bandwidth of the lens-coupled antenna. In contrast, the collimating design places no such limits on the spectrum, at least within the approximations of the calculation described in the text.

Figure 13 Simulated spectral amplitude in the forward direction ($\theta = 0$), for both lens designs, and for several different substrate lens radii. The legend in (a) applies to both (a) and (b). For both lens designs, the spectral bandwidth decreases as the lens radius increases, as a result of the enhancement of the low frequency components. In the hyperhemispherical case, even the smallest lens gives rise to a substantial decrease in amplitude at high frequencies. In the collimating lens, this effect is only evident for the largest lenses.

Figure 14 Directivity of the emitted beam, calculated as described in the text. The open squares and circles show the results for the E-plane, while the crosses and plus signs show the results for the H-plane. The beam from the collimating lens shows a directivity that increases rapidly with increasing frequency, while the hyperhemispherical lens shows little frequency dependence. The solid lines are the directivities for the two lens designs calculated from the simulations shown in

figure 12.

Figure 15 Gaussian beam coupling efficiency, calculated as described in the text, for the E-plane data shown in figure 7. The hyperhemispherical lens design produces a beam that couples more efficiently to a Gaussian mode over much of the relevant bandwidth. This offsets to some degree the lower directivity of the radiation from this lens design.

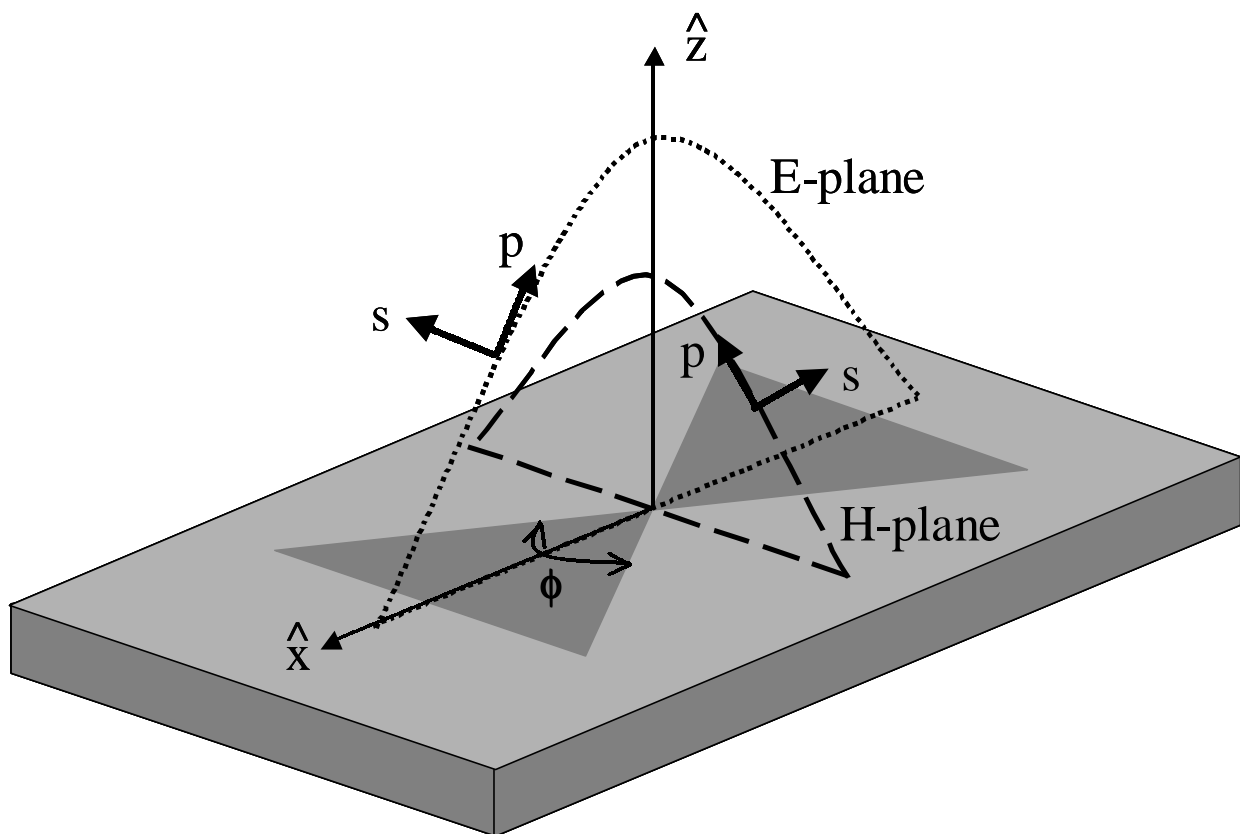
References

- [1] M. C. Nuss and J. Orenstein, "Terahertz time-domain spectroscopy (THz-TDS)," in *Millimeter and sub-millimeter-wave spectroscopy of solids*, G. Grüner, Ed. Heidelberg: Springer-Verlag (1998).
- [2] C. Fattinger and D. Grischkowsky, "Terahertz beams," *Appl. Phys. Lett.*, **54**, 490-492 (1989).
- [3] P. R. Smith, D. H. Auston, and M. C. Nuss, "Subpicosecond photoconducting dipole antennas," *IEEE J. Quant. Elec.*, **24**, 255-260 (1988).
- [4] D. M. Mittleman, R. H. Jacobsen, and M. C. Nuss, "T-ray imaging," *IEEE J. Sel. Top. Quant. Elec.*, **2**, 679-692 (1996).
- [5] J. V. Rudd, D. Zimdars, and M. Warmuth, "Compact, fiber-pigtailed terahertz imaging system," *Proc SPIE*, **3934**, 27-35 (2000).
- [6] M. van Exter and D. Grischkowsky, "Characterization of an optoelectronic terahertz beam system," *IEEE Trans. Microwave Th. Tech.*, **38**, 1684-1691 (1990).
- [7] P. U. Jepsen, R. H. Jacobsen, and S. R. Keiding, "Generation and detection of terahertz pulses from biased semiconductor antennas," *J. Opt. Soc. Am. B*, **13**, 2424-2436 (1996).
- [8] C. Ludwig and J. Kuhl, "Studies of the temporal and spectral shape of terahertz pulses generated from photoconducting switches," *Appl. Phys. Lett.*, **69**, 1194-1196 (1996).
- [9] A. Kaplan, "Diffraction-induced transformation of near-cycle and subcycle pulses," *J. Opt. Soc. Am. B*, **15**, 951-956 (1998).
- [10] A. B. Ruffin, J. V. Rudd, J. F. Whitaker, S. Feng, and H. G. Winful, "Direct observation of the Gouy phase shift with single-cycle terahertz pulses," *Phys. Rev. Lett.*, **83**, 3410-3413 (1999).
- [11] S. Hunsche, S. Feng, H. G. Winful, A. Leitenstorfer, M. C. Nuss, and E. P. Ippen,

- “Spatiotemporal focusing of single-cycle light pulses,” *J. Opt. Soc. Am. A*, **16**, 2025-2028 (1999).
- [12] N. M. Froberg, B. B. Hu, X.-C. Zhang, and D. H. Auston, “Terahertz radiation from a photoconducting antenna array,” *IEEE J. Quant. Elec.*, **28**, 2291-2301 (1992).
- [13] P. Jepsen and S. R. Keiding, “Radiation patterns from lens-coupled terahertz antennas,” *Opt. Lett.*, **20**, 807-809 (1995).
- [14] J. V. Rudd, J. L. Johnson, and D. M. Mittleman, “Quadrupole radiation from terahertz dipoles,” *Opt. Lett.*, **25**, 1556-1558 (2000).
- [15] J. V. Rudd, J. L. Johnson, and D. M. Mittleman, “Cross-polarized angular emission patterns from lens-coupled terahertz antennas,” *J. Opt. Soc. Am. B*, in press (2001).
- [16] D. B. Rutledge and M. S. Muha, “Imaging antenna arrays,” *IEEE Trans. Antennas and Prop.*, **30**, 535-540 (1982).
- [17] D. B. Rutledge, D. P. Neikirk, and D. P. Kasilingam, “Integrated-circuit antennas,” in *Infrared and Millimeter Waves*, vol. 10, K. J. Button, Ed. New York: Academic (1983), pp. 1-90.
- [18] G. M. Rebeiz, “Millimeter-wave and terahertz integrated circuit antennas,” *Proc. IEEE*, **80**, 1748-1770 (1992).
- [19] G. V. Eleftheriades, Y. Brand, J.-F. Zürcher, and J. R. Mosig, “ALPSS: A millimeter-wave aperture-coupled patch antenna on a substrate lens,” *Elec. Lett.*, **33**, 169-170 (1997).
- [20] G. Chattopadhyay, D. Miller, H. G. LeDuc, and J. Zmuidzinas, “A dual-polarized quasi-optical SIS mixer at 550 GHz,” *IEEE Trans. Microwave Th. Tech.*, **48**, 1680-1686 (2000).
- [21] M. van Exter, C. Fattinger, and D. Grischkowsky, “High-brightness terahertz beams characterized with an ultrafast detector,” *Appl. Phys. Lett.*, **55**, 337-339 (1989).

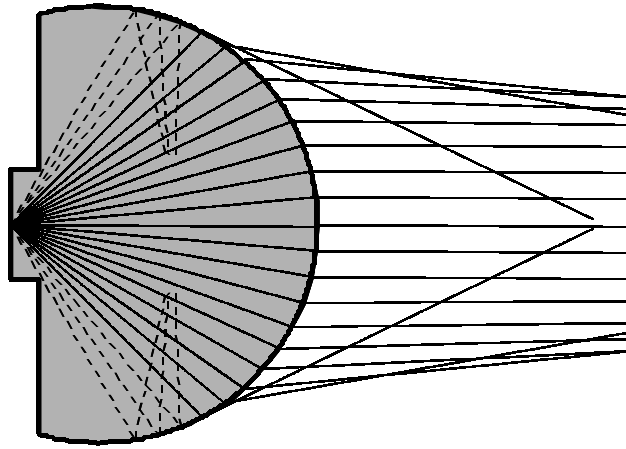
- [22] S.-G. Park, M. R. Melloch, and A. M. Weiner, "Analysis of terahertz waveforms measured by photoconductive and electrooptic sampling," *IEEE J. Quant. Elec.*, **35**, 810-819 (1999).
- [23] M. Born and E. Wolf, *Principles of Optics*, 3rd ed. Oxford: Pergamon Press (1965).
- [24] D. F. Filipovic, S. S. Gearhart, and G. M. Rebeiz, "Double-slot antennas on extended hemispherical and elliptical silicon dielectric lenses," *IEEE Trans. Microwave Th. Tech.*, **41**, 1738-1749 (1993).
- [25] W. B. Dou, G. Zeng, and Z. L. Sun, "Pattern prediction of extended hemispherical lens/objective lens antenna system at millimeter wavelengths," *IEE Proc. Microwave Antennas Prop.*, **145**, 295-298 (1998).
- [26] J. R. Bray and L. Roy, "Performance trade-offs of substrate lens antennas," in *Symposium on Antenna Technology and Applied Electromagnetics (ANTEM, Ottawa, Canada, 1998)*. Vol.
- [27] P. U. Jepsen, "THz radiation patterns from dipole antennas and guided ultrafast pulse propagation," MS Thesis, Fysisk Institut, Odense Universitet, Odense, Denmark (1994).
- [28] W. Lukosz, "Light emission by magnetic and electric dipoles close to a plane dielectric interface. III. Radiation patterns of dipoles with arbitrary orientation," *J. Opt. Soc. Am.*, **69**, 1495-1503 (1979).
- [29] C. R. Brewitt-Taylor, D. J. Gunton, and H. D. Rees, "Planar antennas on a dielectric surface," *Elec. Lett.*, **17**, 729-731 (1981).
- [30] G. H. Brown and O. M. Woodward, "Experimentally determined radiation characteristics of conical and triangular antennas," *RCA Rev.*, **13**, 425-452 (1952).
- [31] R. C. Compton, R. C. McPhedran, Z. Popovic, G. M. Rebeiz, P. P. Tong, and D. B. Rutledge, "Bow-tie antennas on a dielectric half-space: Theory and experiment," *IEEE*

- Trans. Antennas & Propagation*, **35**, 622-631 (1987).
- [32] K. L. Shlager, G. S. Smith, and J. G. Maloney, "Optimization of bow-tie antennas for pulse radiation," *IEEE Trans. Antennas & Propagation*, **42**, 975-982 (1994).
- [33] D. Grischkowsky, S. Keiding, M. van Exter, and C. Fattinger, "Far-infrared time-domain spectroscopy with terahertz beams of dielectrics and semiconductors," *J. Opt. Soc. Am. B*, **7**, 2006-2015 (1990).
- [34] A. Grtler, C. Winnewisser, H. Helm, and P. U. Jepsen, "Terahertz pulse propagation in the near field and the far field," *J. Opt. Soc. Am. A*, **17**, 74-83 (2000).
- [35] R. W. McGowan, G. Gallot, and D. Grischkowsky, "Propagation of ultrawideband short pulses of terahertz radiation through submillimeter-diameter circular waveguides," *Opt. Lett.*, **24**, 1431-1433 (1999).
- [36] S. Hunsche, M. Koch, I. Brener, and M. C. Nuss, "THz near-field imaging," *Opt. Comm.*, **150**, 22-26 (1998).
- [37] B. B. Hu and M. C. Nuss, "Imaging with terahertz waves," *Opt. Lett.*, **20**, 1716-1719 (1995).
- [38] H. Jasik, *Antenna Engineering Handbook*, 1st ed. New York: McGraw-Hill (1961).

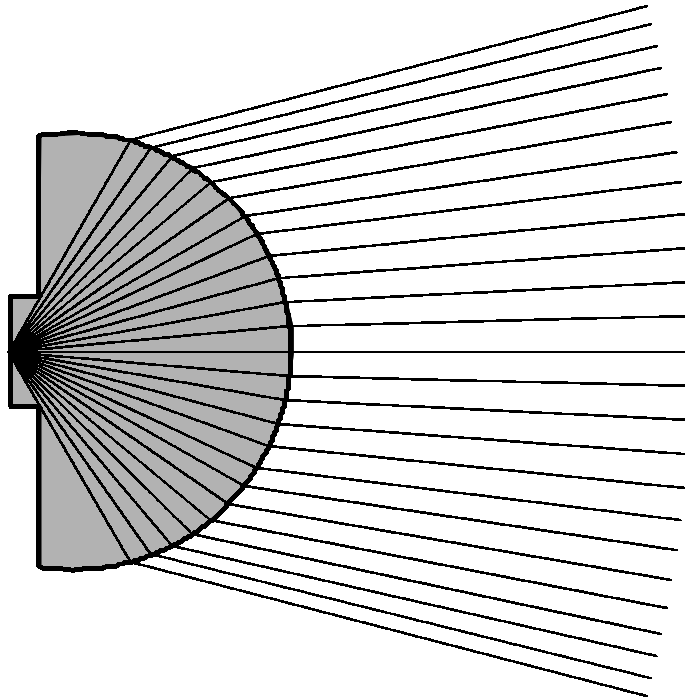


Rudd and Mittleman, figure 1 of 15

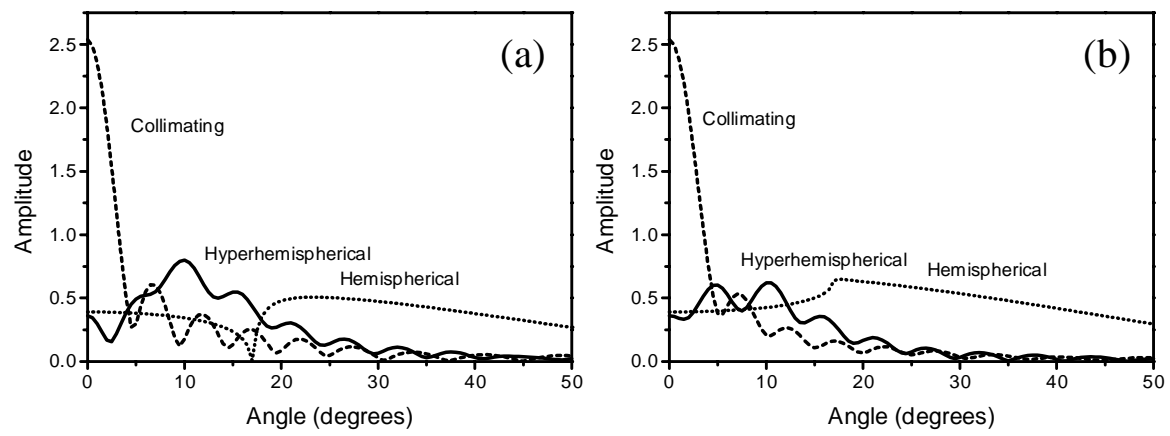
(a)



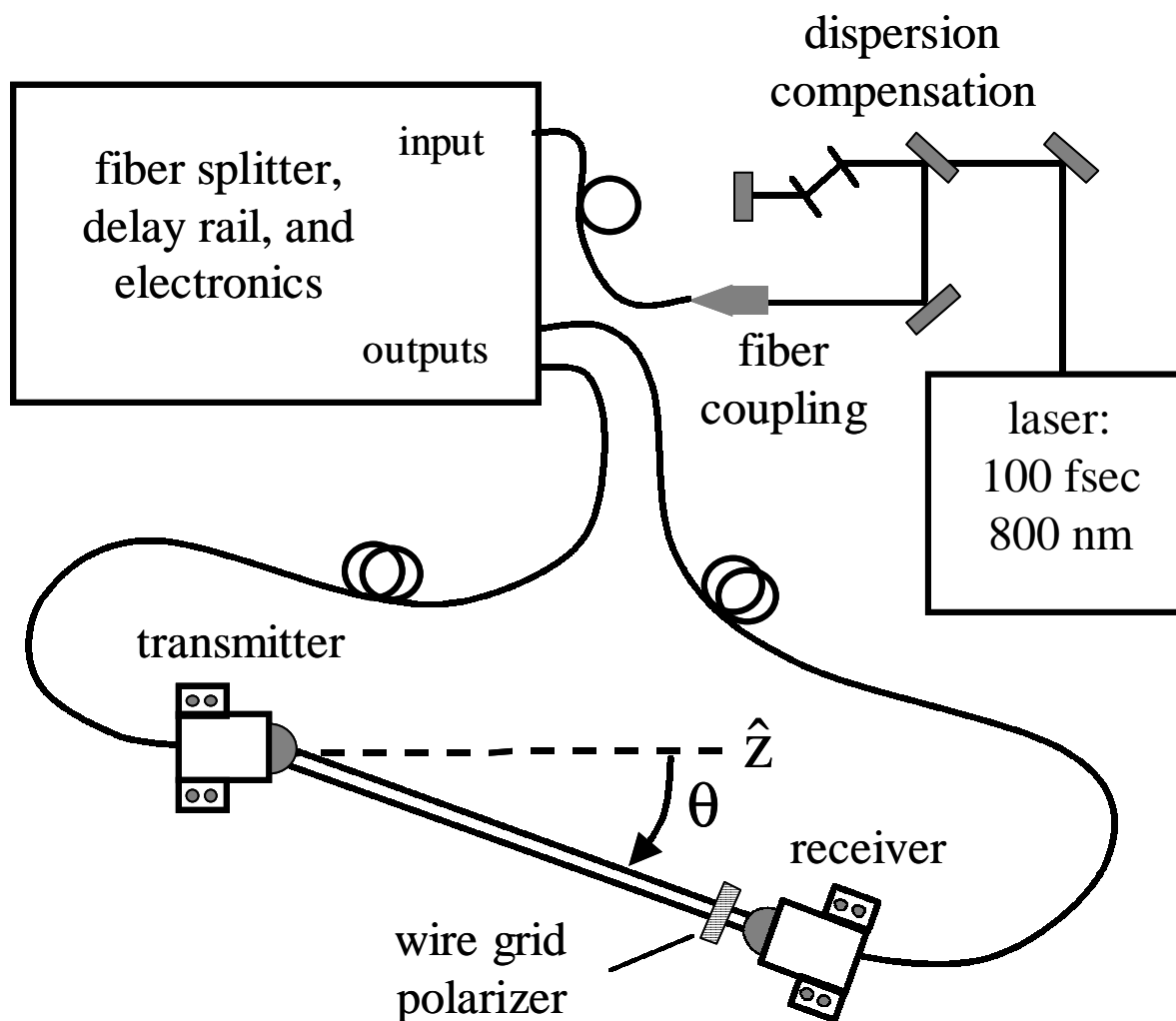
(b)



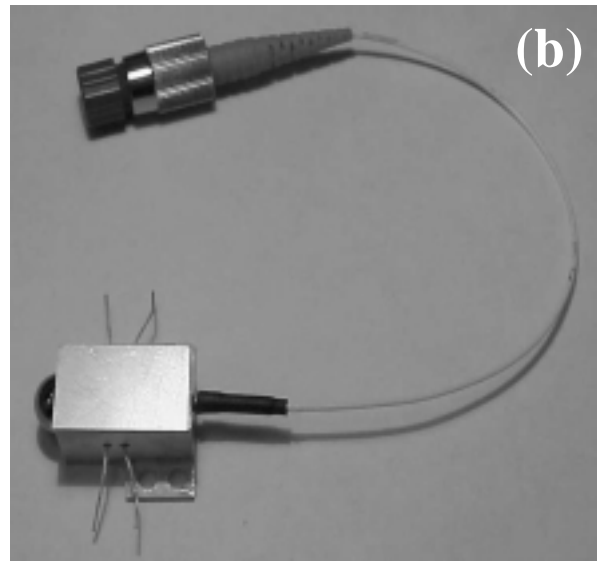
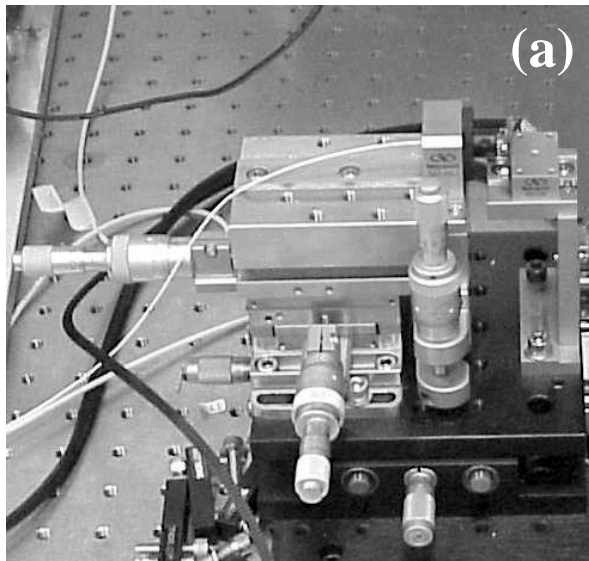
Rudd and Mittleman, figure 2 of 15



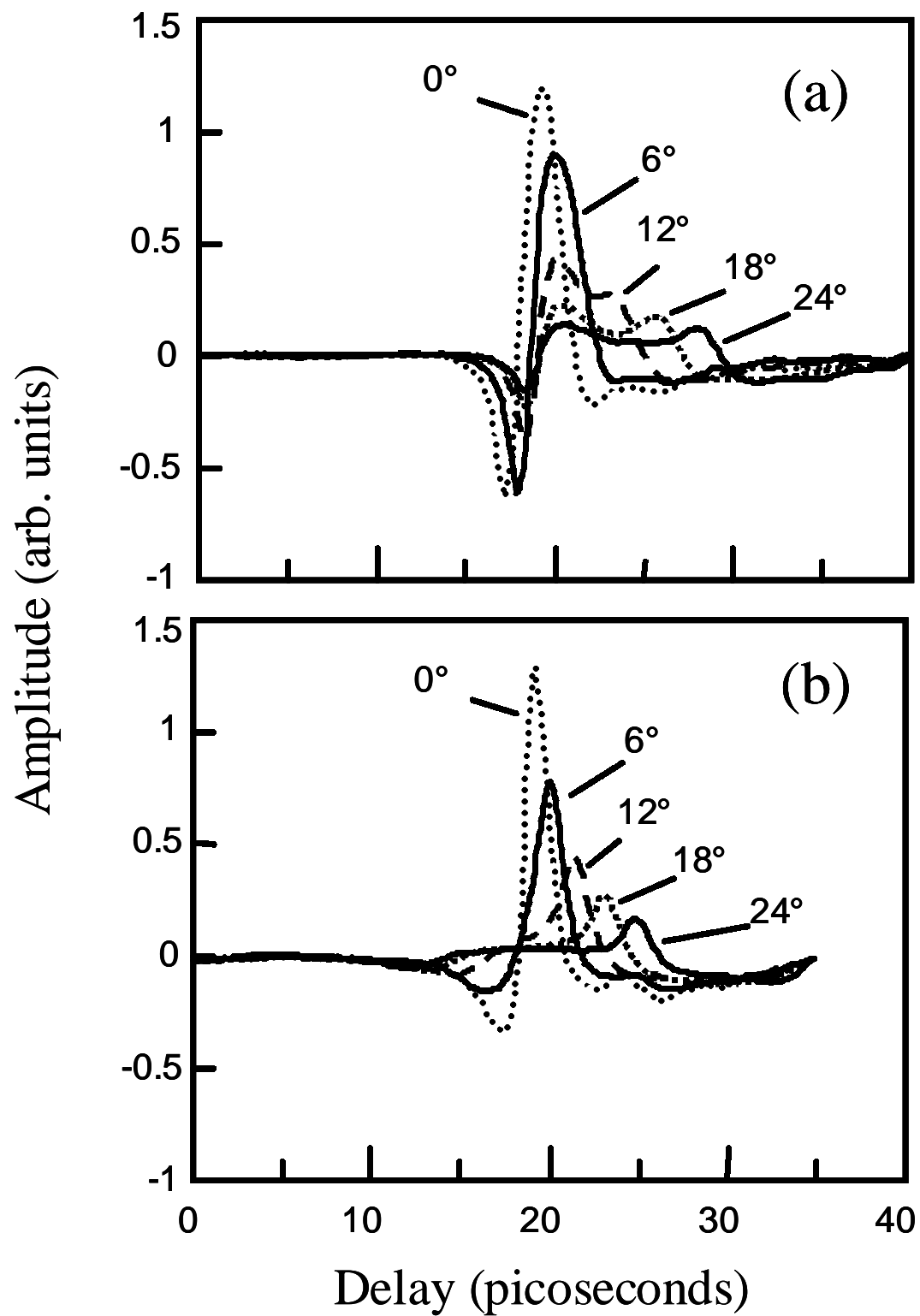
Rudd and Mittleman, figure 3 of 15



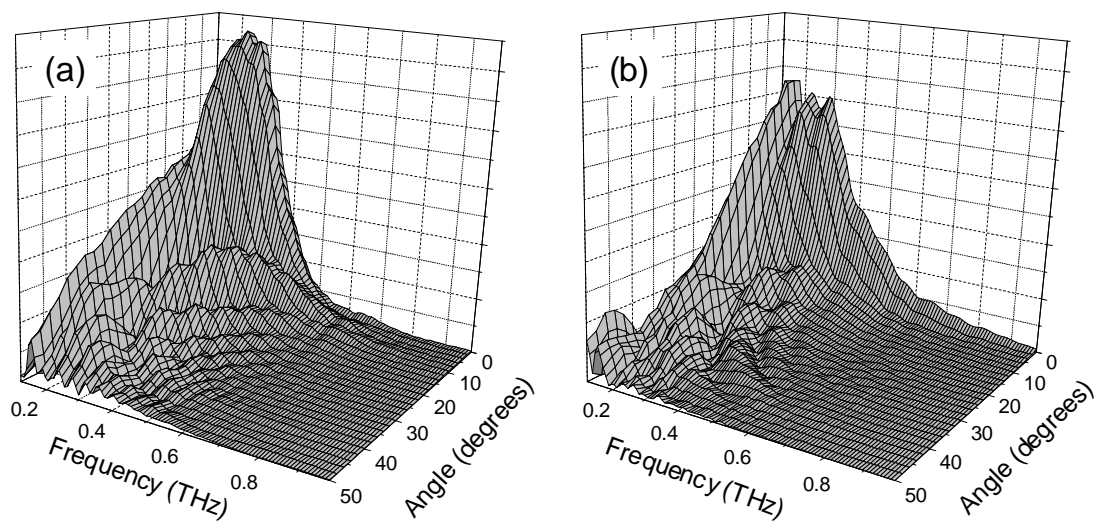
Rudd and Mittleman, figure 4 of 15



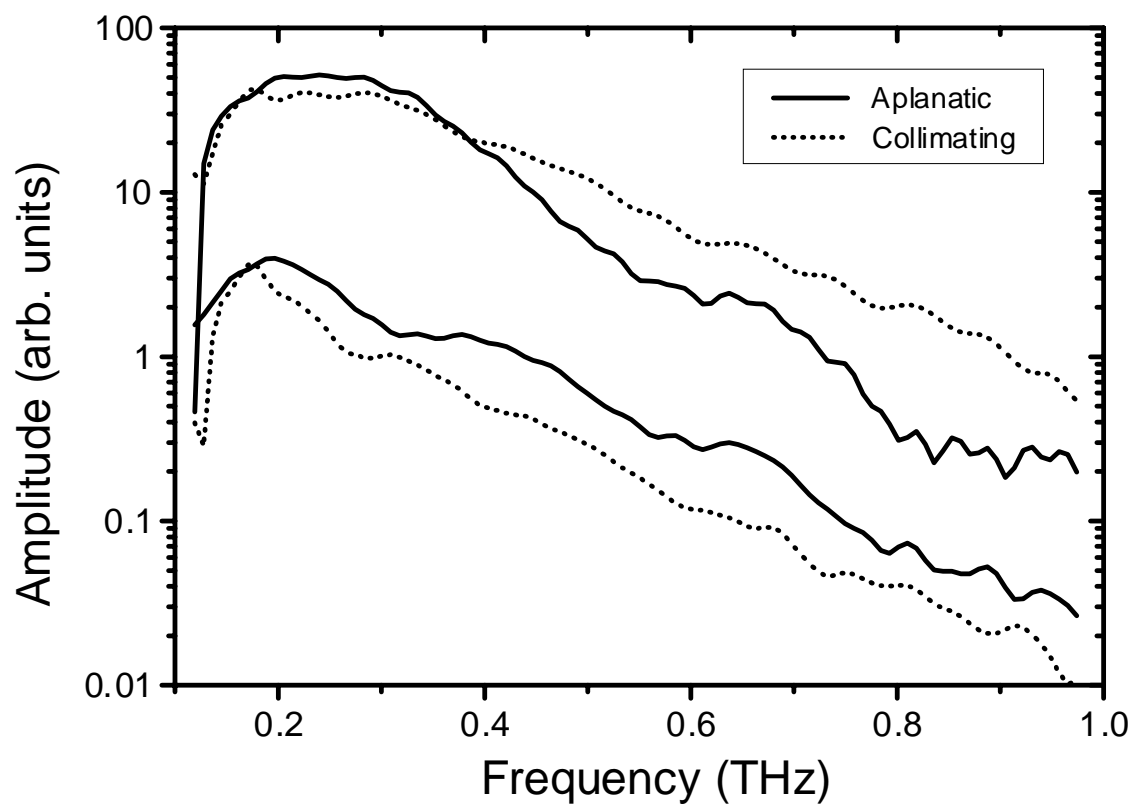
Rudd and Mittleman, figure 5 of 15



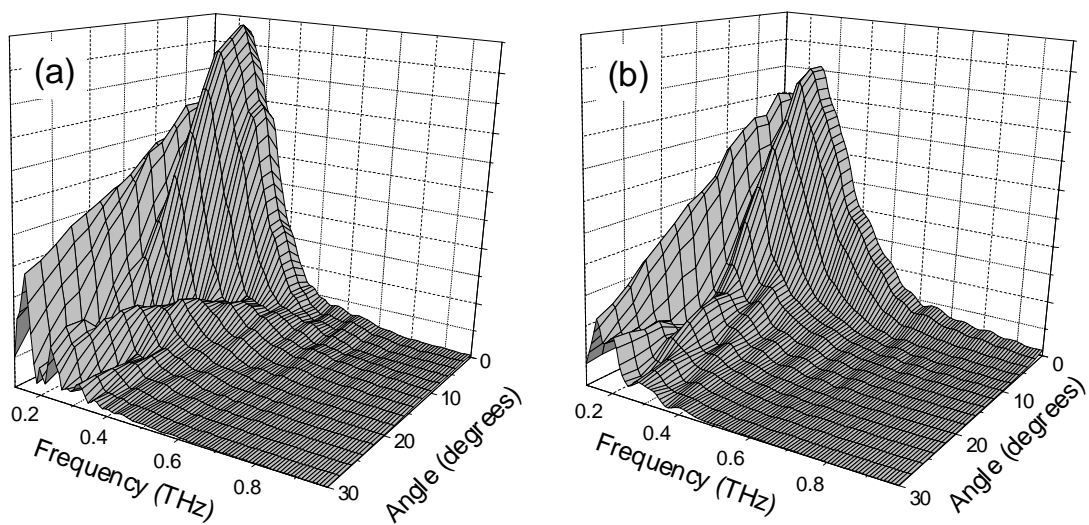
Rudd and Mittleman, figure 6 of 15



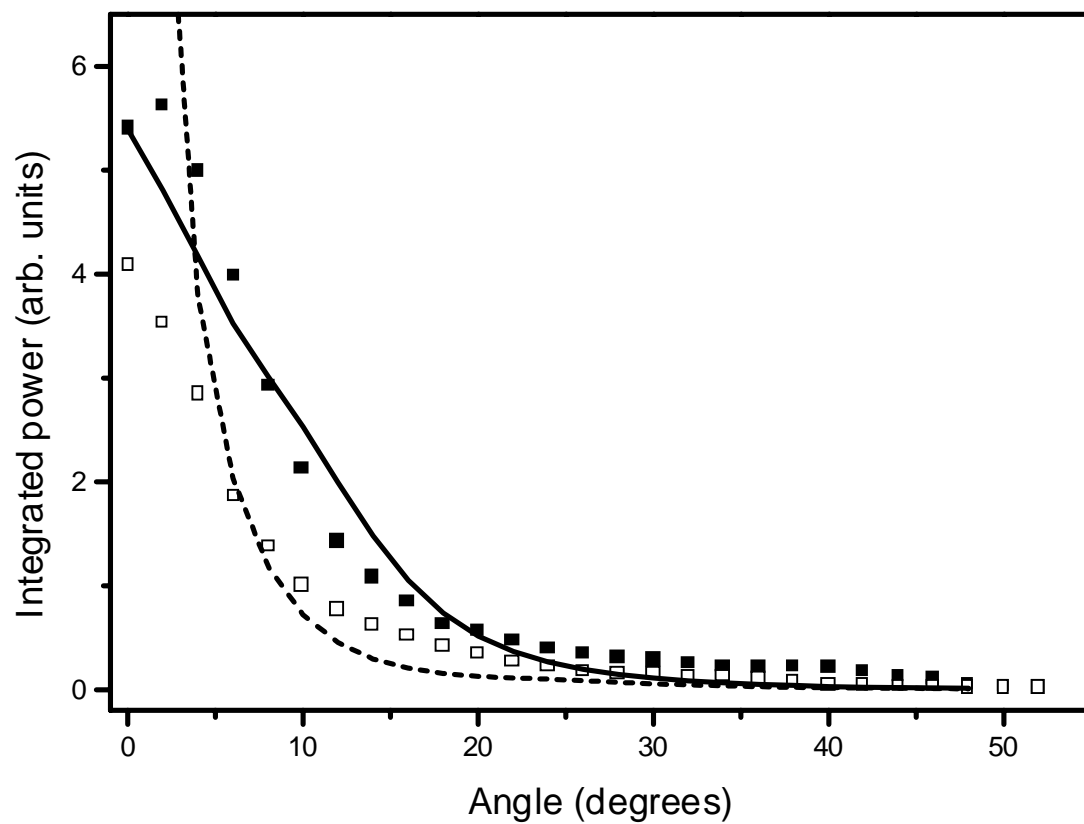
Rudd and Mittleman, figure 7 of 15



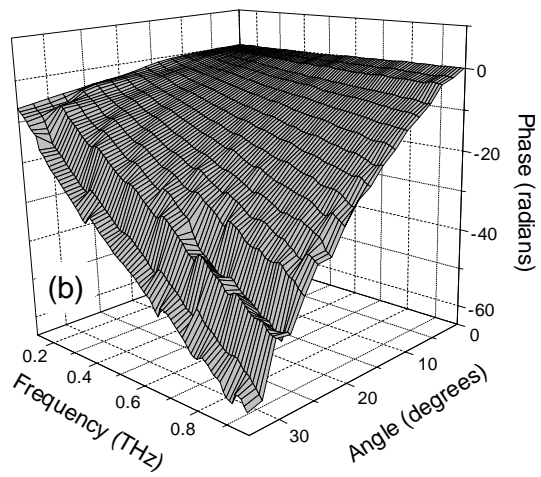
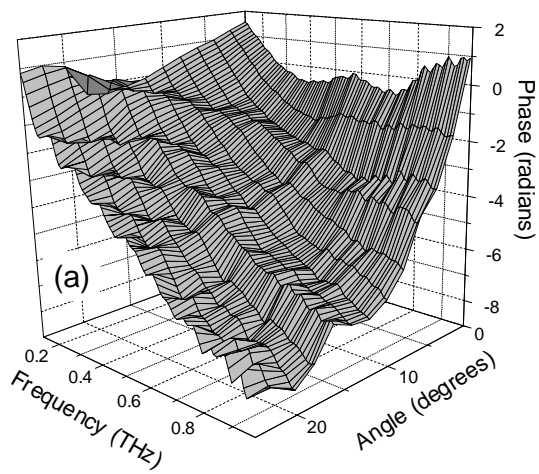
Rudd and Mittleman, figure 8 of 15



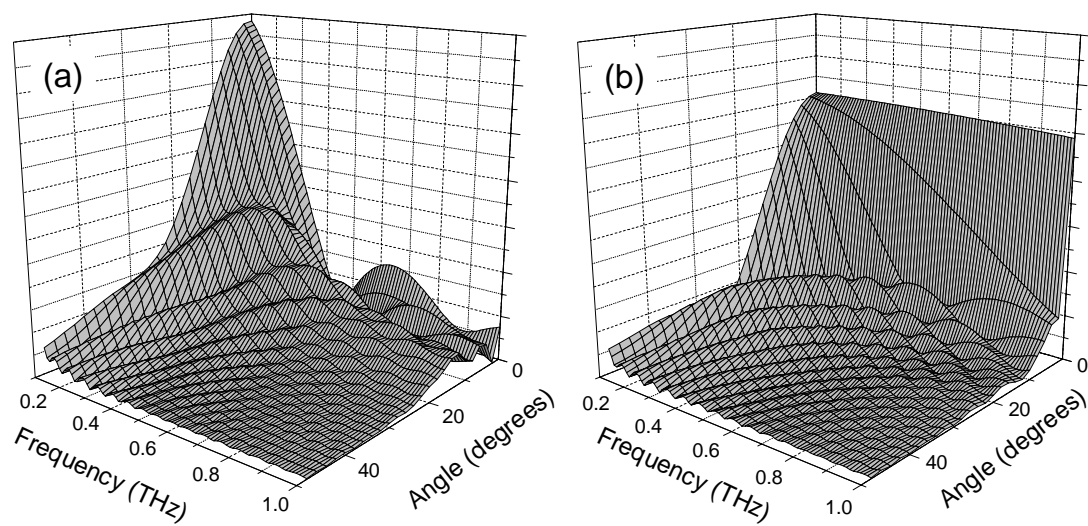
Rudd and Mittleman, figure 9 of 15



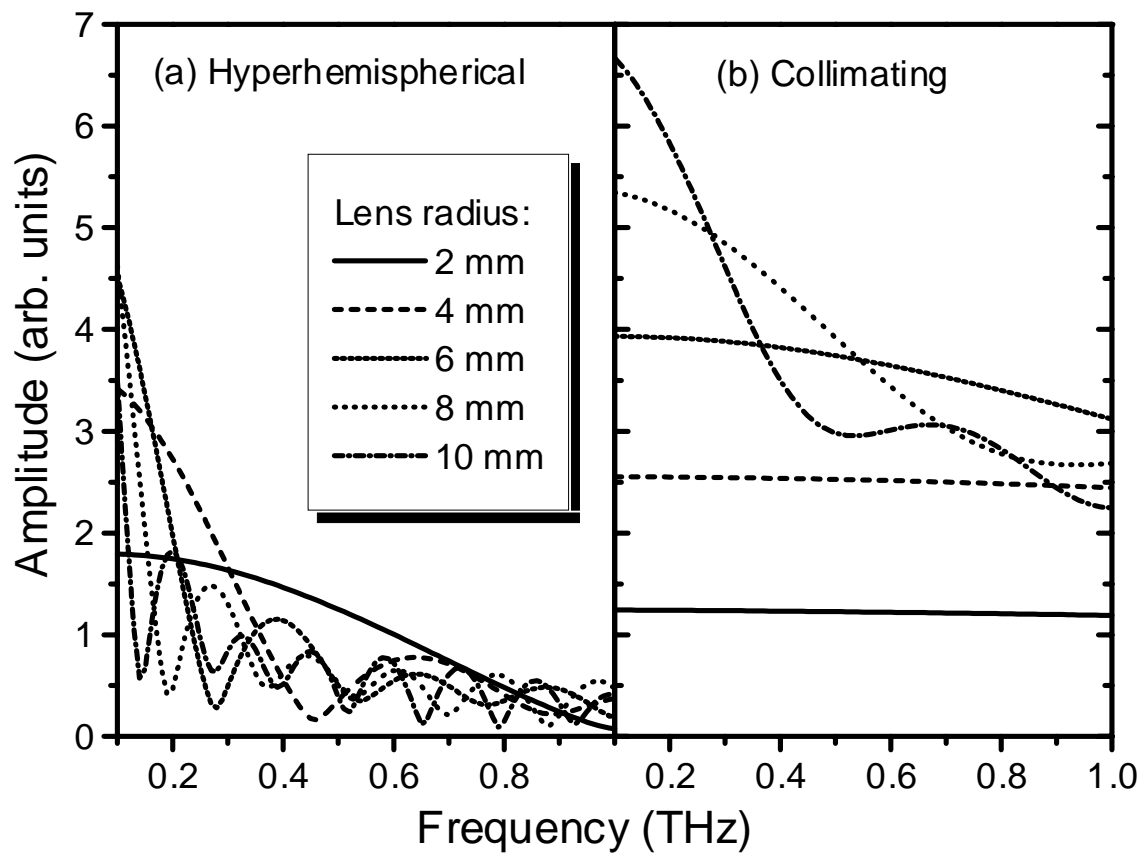
Rudd and Mittleman, figure 10 of 15



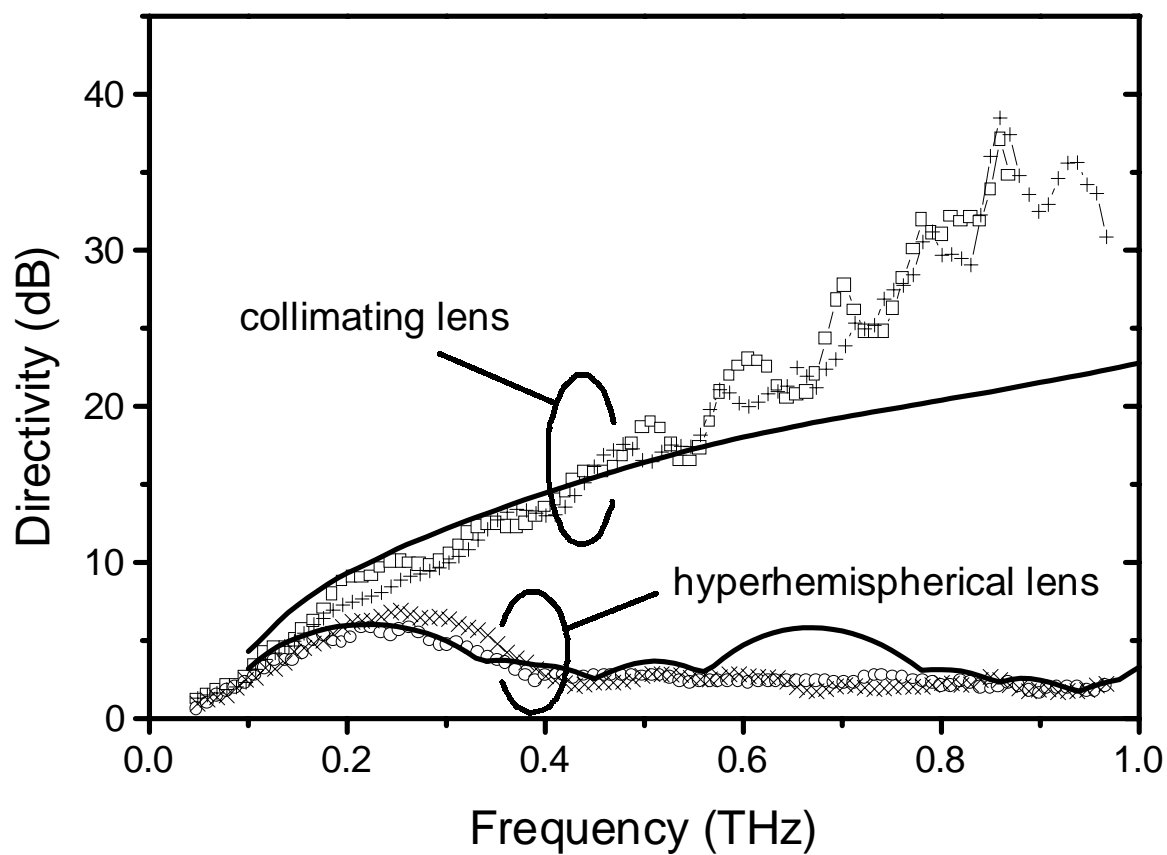
Rudd and Mittleman, figure 11 of 15



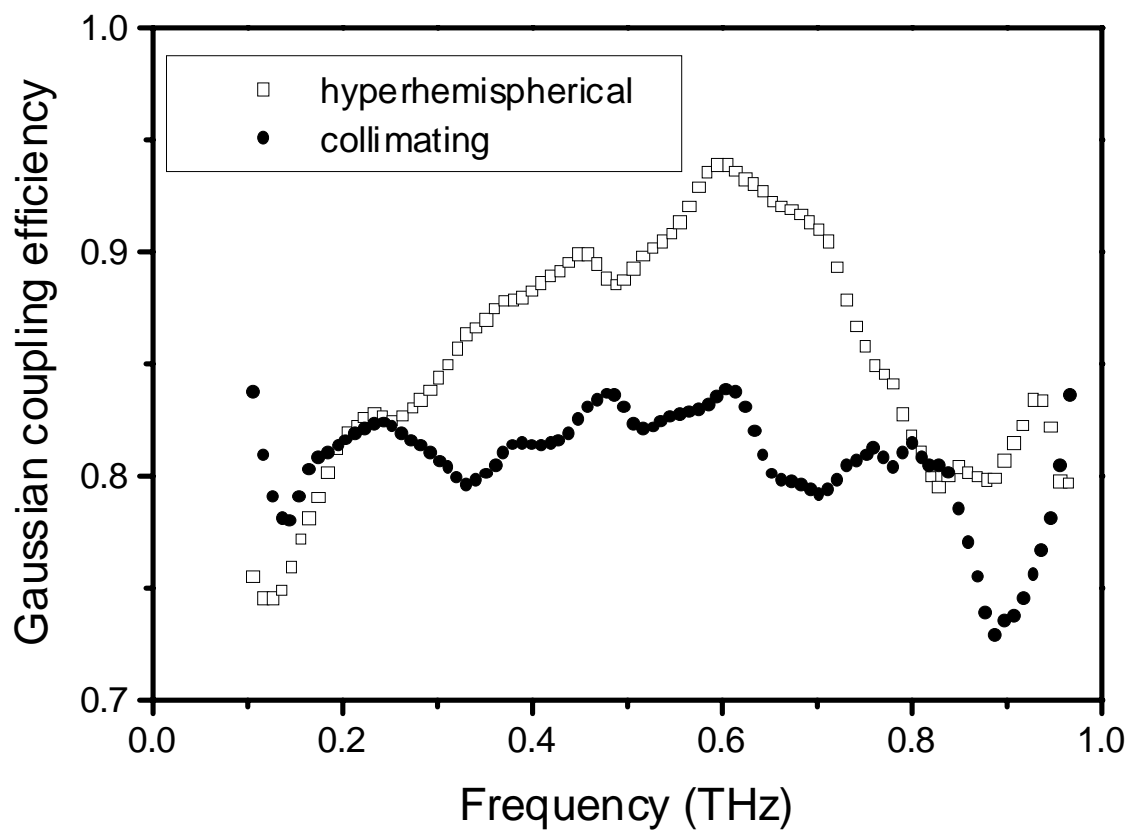
Rudd and Mittleman, figure 12 of 15



Rudd and Mittleman, figure 13 of 15



Rudd and Mittleman, figure 14 of 15



Rudd and Mittleman, figure 15 of 15